1 **Revision 1**

2 **Sound Velocities of Iron-Nickel ($Fe_{90}Ni_{10}$) Alloy up to 8 GPa and 773 K: The Effect of**
3 **Nickel on the Elastic Properties of bcc-Iron at High *P-T***

4

5 **Siheng Wang[1,*], Nao Cai[2,†], Xintong Qi[2], Sibo Chen[1], and Baosheng Li[1,2]**

6

7 [1]Department of Geosciences, Stony Brook University, Stony Brook, NY 11794, USA

8 [2]Mineral Physics Institute, Stony Brook University, Stony Brook, NY 11794, USA

9

10 *Corresponding author: Siheng Wang (siheng.wang@stonybrook.edu), Department of
11 Geosciences, Stony Brook University, Stony Brook, NY 11794, USA

12 †Current addresses: College of Earth and Planetary Sciences, University of Chinese Academy of
13 Sciences, Beijing, China.

Abstract

Sound velocities of iron and iron-based alloys at high pressure and high temperature are crucial for understanding the composition and structure of Earth's and other telluric planetary cores. In this study, we performed ultrasonic interferometric measurements of both compressional (V_P) and shear (V_S) velocities on a polycrystalline body-centered-cubic (bcc)-$Fe_{90}Ni_{10}$ up to 8 GPa and 773 K. The elastic moduli and their pressure and temperature derivatives are derived from least square fits to third-order finite strain equations, yielding K_{S0} = 154.2(8) GPa, G_0 = 73.2(2) GPa, K_{S0}' = 4.6(2), G_0' = 1.5(1), $\partial K_S/\partial T$ = -0.028(1) GPa/K, and $\partial G/\partial T$ = -0.023(1) GPa/K. A comparison with literature data on bcc-Fe suggests that nickel not only decreases both P and S wave velocities but also weakens the temperature effects on the elastic moduli of Fe-Ni alloys.

Key words: Fe-Ni alloy; sound velocity; high pressure and high temperature; ultrasonic interferometry

1. Introduction

Understanding the nature of Earth's core, which is the least accessible region of the Earth, is one of the most challenging tasks in geophysical research. Seismic waves can travel inside the Earth and serve as a powerful tool to probe the physical properties of Earth's interior, such as the density, compressional (P) and shear (S) wave velocities depth profiles; see for example the Preliminary Reference Earth Model (Dziewonski and Anderson 1981). Comparing seismic results with lab-based mineral physics investigations, as well as other evidence from geochemical and cosmochemical studies, it has been widely accepted that Earth's core is composed of iron alloyed with approximately 10 wt.% nickel and several percent of light elements (such as Si, O, H, S, C, etc.) (e.g., Birch 1952, 1964; Li and Fei 2014; Mcdonough and Sun 1995). However, direct studies on the behavior and elasticity properties of iron alloys at high pressure and high temperature are still scarce.

Iron-nickel alloys can exist in several crystallographic structures: body-centered-cubic (bcc) structure (α phase), face-centered cubic (fcc) structure (γ phase), and hexagonal close-packed (hcp) structure (ε phase), etc., depending on the pressure (P) and temperature (T) conditions and the nickel concentration (**Fig. 1**). At ambient conditions, iron crystallizes in bcc structure while nickel prefers the fcc structure; when the nickel concentration exceeds ~20 wt.%, Fe-Ni alloys will gradually transform from bcc to fcc structure. However, there is no conclusive consensus on the phase diagram of Fe-Ni systems at high pressure and high temperature (e.g., Dubrovinsky et al. 2007; Kuwayama et al. 2008; Mao et al. 1990; Sakai et al. 2011; Tateno et al. 2012; Tateno et al. 2010). While there are several experimental and theoretic predictions arguing that the bcc structure could be the stable phase (e.g., Dubrovinsky et al. 2007; Vocadlo et al. 2003) at Earth's core conditions, these predictions were not supported by later experiments (e.g., Sakai et al. 2011;

Tateno et al. 2012; Tateno et al. 2010). The more recent calculations by Stixrude (2012) demonstrate a wide stability field of hcp Fe to 23 Mbar (2,300 GPa) and 19,000 K, supporting the later high *P-T* experiments. With the complexity of alloying with light elements, the phase diagram is even more controversial. Thus, more information about the physical and chemical properties (such as, density, sound velocity, bulk modulus, shear modulus, anisotropy, etc.) of the different phases of the Fe-Ni alloys are needed to further constrain the composition and structure of the Earth's core.

Sound velocities of pure iron (Fe) have been experimentally accessed by ultrasonic interferometry (UI), inelastic X-ray scattering (IXS), nuclear resonant inelastic X-ray scattering (NRIXS), and laser pulses (LP), etc.] at room temperature (e.g., Chigarev et al. 2008; Decremps et al. 2014; Fiquet et al. 2001; Gleason et al. 2013; Mao et al. 1998; Murphy et al. 2013) and high temperature (e.g., Antonangeli et al. 2012; Lin et al. 2005; Liu et al. 2014; Mao et al. 2012; Ohtani et al. 2013; Shibazaki et al. 2016). In contrast, experimental studies on the sound velocity of iron-nickel (Fe-Ni) alloys are still limited (Kantor et al. 2007; Lin et al. 2003; Morrison et al. 2019; Wakamatsu et al. 2018), especially for the shear properties under simultaneous high pressure and high temperature conditions.

In the present study, we have carried out ultrasonic interferometric (UI) measurements on a polycrystalline bcc-$Fe_{90}Ni_{10}$ sample at simultaneous pressure and temperature conditions. Compared to other sound velocity measurement techniques, UI in large volume apparatus embeds the advantages of stable and uniform heating of sample and direct measurement of both P and S wave velocities simultaneously. We applied a third-order finite strain approach for data analysis; the resultant compressional and shear velocities as well as the bulk and shear moduli

for bcc-$Fe_{90}Ni_{10}$ are compared with those for pure iron to evaluate the effects of nickel content on the elastic properties of Fe-Ni alloys.

2. Experimental methods

The polycrystalline sample of $Fe_{90}Ni_{10}$ (10 wt.% Nickel) was a cylindrical disk cut from a rod purchased from Princeton Scientific Cooperation. Before the ultrasonic measurements, the sample was annealed at 3 GPa, 773 K. Scanning electron microscope (SEM) analysis was conducted on the recovered sample and the results (**Fig. 2**) indicated that the sample was homogenous with an average grain size less than 1 μm. There was no detectable oxygen observed in the Energy-dispersive X-ray spectroscopy (EDS), suggesting that no oxidation reactions occurred during the high temperature annealing process.

To optimize the acoustic signals in the ultrasonic measurement, both sides of the sample were polished using diamond lapping film to 1 μm. The final dimensions of the polished sample were 0.930(2) mm in length and 2.010(2) mm in diameter, with a bulk density of 7.95(3) g/cm^3, as obtained by the Archimedes' method.

High pressure and high temperature ultrasonic measurements were performed to about 8 GPa, 773 K in a 2000-ton uniaxial split-cylinder apparatus (USCA-2000) in the High-Pressure Lab at Stony Brook University. A sketch of the 14/8 cell assembly used in this study is shown in **Fig. 3**. A dual mode $LiNbO_3$ transducer (10º Y-cut) was used to generate and receive both the compressional wave and shear wave simultaneously (50 MHz resonant frequency for P waves and 30 MHz for S waves). A dense alumina rod was placed on the top of the sample and served as the acoustic buffer rod. Due to the low yield strength of NaCl at high temperatures, a disk of NaCl was placed at the back of the sample to provide a pseudo-hydrostatic environment during

the experiment (Li et al. 2001). The high temperature environment was generated by a graphite heater and monitored by W/Re5%-W/Re26% type-C thermocouples. The thermocouple junction was placed at a location that mirrors the center of the sample position relative to the center of the high-pressure cell. Even though they were not directly in contact with each other, the thermocouple reading is believed to closely represent the sample temperatures at high pressure. The temperature measurement uncertainty in current experiment is approximately ±10 K. P and S wave travel times were acquired using the transfer function technique and analyzed using the pulse echo overlap (PEO) method by overlapping the buffer rod and sample echoes (**Fig. 4**). Details about the transfer function technique for data acquisition and processing have been discussed elsewhere (Li et al. 2002; Li et al. 2004). Cell pressures were calculated from the shear wave travel times of the alumina buffer rod using the pressure scale at high temperature by equation:

$$P = 242.5(9) \times \left(1 - t_{S\_bf}/t_{S0\_bf}\right) + 0.01099(5) \times (T - T_0) \quad (1.)$$

where P is cell pressure, t_{S_bf} is the S wave travel time of the buffer rod, and t_{S0_bf} is the S wave travel time at ambient conditions (for further details of the use of alumina as a pressure marker, see Wang et al. 2015). The details of the experimental data on buffer rod are listed in supplementary **Table S1**. The pressure uncertainty is estimated to be around ±0.2 GPa in current study.

The experimental *P-T* path is shown in the **Fig. 1**, superimposed with the previously determined phase diagram from the diamond anvil cell (DAC) experiments (Huang et al. 1988). The sample was first compressed at room temperature to a maximum pressure of ~8 GPa, followed by heating to a peak temperature of 773 K to release the deviatoric stress in the cell, then the

ultrasonic data were collected at 100 K intervals along cooling paths to room temperature while the sample was under nearly hydrostatic environment (Li et al. 2001). Multiple heating and cooling cycles were performed during decompression to provide a dense coverage of experimental data in *P-T* space. The P and S wave travel times were obtained at 35 and 27 MHz, respectively, in this study, to maximize the signal-to-noise ratio.

3. Data analyses

After the experiment, the sample length and diameter were 0.926(2) mm and 2.010(5) mm respectively, indicating that, within 0.4% uncertainty, the sample can be considered to have undergone elastic compression under pseudo-hydrostatic conditions during the entire course of the experiment. As indicated by the P and S wave signals obtained at 7.6 GPa and 776 K in **Fig. 4**, the reflections from the front (buffer rod/sample) and rear (sample/backing) surfaces are highly distinguishable from the background, providing a reliable measurements of travel times with 0.1-0.6% in precision.

The travel time results at all experimental conditions from this study are summarized in **Table 1**. As shown in previous studies, velocities (V_P and V_S), and elastic moduli (K_S and G) as well as their pressure and temperature derivatives (K_S, G, K_S', G', $\partial K_S/\partial T$, and $\partial G/\partial T$) can be obtained by a third-order finite strain approach (Davies and Dziewonski 1975; Li and Zhang 2005).

First, because the sample has undergone nearly hydrostatic deformation during cooling along decompression the experiment, it is reasonable to assume that density (ρ), volume (V), and length (l) have the following relationships:

$$\frac{\rho}{\rho_0} = \frac{\mathrm{V}_0}{\mathrm{V}} = \left(\frac{l_0}{l}\right)^3 \qquad (2.)$$

This is the peer-reviewed, final accepted version for American Mineralogist, published by the Mineralogical Society of America.
The published version is subject to change. Cite as Authors (Year) Title. American Mineralogist, in press.
DOI: https://doi.org/10.2138/am-2021-7716. http://www.minsocam.org/

The elastic properties at high pressure and temperature can be calculated through the sound velocities $V_{(P,S)} = \frac{2l}{2t_{(P,S)}}$ and densities ρ by the relationships $K_S = \rho(V_P^2 - \frac{4}{3}V_S^2)$ and $G = \rho V_S^2$ for the bulk and shear modulus, respectively. Under adiabatic compression, the finite strain equations are expressed as the following:

$$\rho V_P^2 = (1-2\varepsilon)^{\frac{5}{2}}(L_1 + L_2\varepsilon) \quad (3.)$$

$$\rho V_S^2 = (1-2\varepsilon)^{\frac{5}{2}}(M_1 + M_2\varepsilon) \quad (4.)$$

$$K_{S(0,T)} = L_1 - \frac{4}{3}M_1 \quad (5.)$$

$$G_{(0,T)} = M_1 \quad (6.)$$

$$K'_{S(0,T)} = \frac{5L_1 - L_2}{3K_{S(0,T)}} - \frac{4G'_{(0,T)}}{3} \quad (7.)$$

$$G'_{(0,T)} = \frac{5M_1 - M_2}{3K_{S(0,T)}} \quad (8.)$$

where the subscript (P,T) indicates values at the pressure P and temperature T, and the Eulerian strain $\varepsilon = \frac{1}{2}\left[1 - \left(\frac{\rho_{(P,T)}}{\rho_{(0,T_{foot})}}\right)^{2/3}\right]$ (The T_{foot} here refers to the foot temperature of an adiabat at ambient pressure and T refers to the temperature along this adiabat at pressure P). All temperatures reached in the entire experiment are assumed to be raised along separate adiabats from different foot temperatures T_{foot}. Thus, the adiabatic foot temperature for each data point as well as the corresponding density and elastic properties at ambient pressure and T_{foot} can be extracted through the following equations:

$$\left(\frac{\partial T}{\partial P}\right)_S = \frac{\gamma T}{K_S} \quad (9.)$$

This is the peer-reviewed, final accepted version for American Mineralogist, published by the Mineralogical Society of America.
The published version is subject to change. Cite as Authors (Year) Title. American Mineralogist, in press.
DOI: https://doi.org/10.2138/am-2021-7716. http://www.minsocam.org/

$$\rho_{(0,T_{foot})} = \rho_{(0,T_0)} e^{-\int \alpha dT} \quad (10.)$$

$$K_{S(0,T_{foot})} = K_{S(0,T_0)} + (T_{foot} - T_0)\left(\frac{\partial K_S}{\partial T}\right)_P \quad (11.)$$

$$G_{(0,T_{foot})} = G_{(0,T_0)} + (T_{foot} - T_0)\left(\frac{\partial G}{\partial T}\right)_P \quad (12.)$$

$$K'_{SS(0,T_{foot})} = K'_{SS(0,T_0)} + (T_{foot} - T_0)\left(\frac{\partial^2 K_S}{\partial P \partial T}\right)_P + \left(\frac{\partial K_S}{\partial T}\right)_P \frac{\gamma T}{K_S} \quad (13.)$$

$$G'_{S(0,T_{foot})} = G'_{S(0,T_0)} + (T_{foot} - T_0)\left(\frac{\partial^2 G}{\partial P \partial T}\right)_P + \left(\frac{\partial G}{\partial T}\right)_P \frac{\gamma T}{K_S} \quad (14.)$$

$$P = -3K_{S(0,T_{foot})}(1-2\varepsilon)^{5/2}\left(1 + \frac{3}{2}(4 - K'_{SS(0,T_{foot})})\varepsilon\right)\varepsilon \quad (15.)$$

The sample lengths, as well as the thermoelastic properties K_S, G, K_S', G', $\partial K_S/\partial T$, $\partial G/\partial T$ at ambient conditions, were refined using a least-square fit by minimizing the difference between the observed compressional and shear velocities ($V_{(P,S)} = \frac{2l}{2t_{(P,S)}}$) and pressures from **Eq.(1)** with those calculated by finite strain theory [**Eqs. (3), (4), and (15)**]. More details about the data analysis procedures can be found elsewhere (Li and Zhang 2005). In the *P-T* range of the current experiment, the thermal expansivity α was assumed to be a constant value of 4.67×10^{-5} (Zhang and Guyot 1999); the Grüneisen parameter γ was constrained by the assumption of $\rho\gamma$ = constant with γ_0 = 1.65 (Quareni and Mulargia 1988); cross derivatives $(\partial^2 K_S/\partial P\partial T)_P$ and $(\partial^2 G/\partial P\partial T)_P$ were assumed to be zero in the current *P-T* range. The minimization usually takes only a few iterations to achieve convergence, and the results for the elastic properties are shown in **Table 2**.

This is the peer-reviewed, final accepted version for American Mineralogist, published by the Mineralogical Society of America.
The published version is subject to change. Cite as Authors (Year) Title. American Mineralogist, in press.
DOI: https://doi.org/10.2138/am-2021-7716. http://www.minsocam.org/

4. Results and discussion

According to **Fig. 1**, some of our experimental data were collected close to the bcc-fcc boundary or within the stability filed of the fcc phase of $Fe_{90}Ni_{10}$ as suggested by DAC experiments from Huang et al. (1988). However, a recent electrical resistivity measurement in the large volume press with a similar experimental setup as current study suggested the bcc-to-fcc phase transition of $Fe_{90}Ni_{10}$ would not occur until ~900 K at the pressure range of 4.5 GPa and 8 GPa (Pommier 2020). A close examination of the recorded waveforms as well as the subsequent analysis of P and S wave travel times did not suggest a phase transition to fcc phase in our *P-T* range. This was further tested by performing a separate fit without the data at 773 K. As indicated by the results shown in **Table 2,** within the uncertainty, the inclusion of the data at 773 K has an insignificant effect on the fitting results and can be reliably treated as the representative values for the bcc phase.

The compressional and shear wave velocities data obtained in this study are compared in **Fig. 5** with those from ultrasonic measurements (Shibazaki et al. 2016) and an IXS study on bcc-Fe (Liu et al. 2014), as well as data from NRIXS studies on both bcc-Fe and bcc-$Fe_{91}Ni_{09}$ (Morrison et al. 2019). At room temperature, the velocities of both P and S waves for bcc-$Fe_{90}Ni_{10}$ are consistently lower than pure Fe from Shibazaki et al. (2016) by 5% and 6%, respectively, which is in good agreement with the ~6% velocity depression observed in NRIXS studies on Fe-Ni alloys with 0 and 9 at.% (which corresponding to ~10 wt.%) nickel (Morrison et al. 2019). However, the absolute values for both P and S waves from NRIXS are systematically lower than those from other techniques (UI, IXS), which could be attributed to the fact that NRIXS is based on the Debye model to analyze the data instead of measuring the sound velocity directly. Comparing to those for bcc-Fe from Shibazaki et al. (2016), V_P of bcc-$Fe_{90}Ni_{10}$ from current

study exhibits a slower rate of increase with pressure [~5.1×10^{-2} km/s/GPa versus (*vs.*) 6.9×10^{-2} km/s/GPa for $Fe_{90}Ni_{10}$ and Fe, respectively] while V_S increases at a relatively similar rate (~2.1×10^{-2} km/s/GPa *vs.* 2.0×10^{-2} km/s/GPa for $Fe_{90}Ni_{10}$ and Fe, respectively).

With increasing temperature, both V_P and V_S decrease within the entire *P-T* range of the current experiment with a larger reduction in V_S than V_P. For example, at ~3 GPa, the depressions in V_P and V_S from 300 K to 800 K are 4%, 7% for $Fe_{90}Ni_{10}$ and 6%, 8% for pure Fe, respectively. The compressional velocity (V_P) decrease from 300 to 700 K reported by Liu et al. (2014) is about 5%, which is larger than the 4% for bcc-$Fe_{90}Ni_{10}$ observed in current study. In addition, nonlinear elastic anomalies indicative of a magnetic transition at high temperature (e.g., Dever 1972) were not observed in the current study, which could possibly be explained by the limited temperature range (300-773 K).

The adiabatic bulk modulus (K_S) and shear modulus (G) calculated in current study are plotted in **Fig. 6** as a function of pressure and temperature. **Table 2** is a comparison of the thermoelastic properties of Fe and Fe-Ni alloys obtained from this study and previous experimental studies. Note in this table that our study reports for the first time the temperature dependences of the elastic bulk and shear moduli ($\partial K_S/\partial T$ and $\partial G/\partial T$) of bcc-$Fe_{90}Ni_{10}$. Comparing with previous ultrasonic studies listed in **Table 2**, the bulk and shear moduli of bcc-$Fe_{90}Ni_{10}$ at ambient conditions [K_{S0} = 154.2(8) GPa and G_0 = 73.2(2) GPa] are lower than those values of bcc-Fe (K_{S0} = 165-168 GPa and G_0 = 78-82 GPa) by approximately 7% and 9%, respectively (Adams et al. 2006; Dever 1972; Isaak and Masuda 1995; Leese and Lord Jr 1968; Shibazaki et al. 2016). The effect of nickel content on bulk modulus observed in this study is consistent with previous

suggestions based on pressure-volume (*P-V*) measurements in DAC (Morrison et al. 2018; Takahashi et al. 1968).

It is also worthwhile to note that, comparing with pure bcc-Fe (Shibazaki et al. (2016), bcc-$Fe_{90}Ni_{10}$ exhibits a weaker pressure dependence of K_S than bcc-Fe (**Fig. 6**), which can be quantified by the pressure derivative K_S' [4.6(2) for bcc-$Fe_{90}Ni_{10}$ vs. 6.75(33) for pure Fe]; meanwhile for the shear modulus, bcc-$Fe_{90}Ni_{10}$ and bcc-Fe show close agreement with each other in their pressure derivatives [G_0' = 1.5(1) vs. 1.66(14), respectively]. These comparisons are believed to reveal primarily the intrinsic difference resulted from nickel substitution in the alloy; the different pressure calibration method used in the current experiments (alumina pressure gauge) and those of Shibazaki et al. (2016) [equation of state (EOS) of MgO + hBN] may also contribute, but are not considered to be an appreciable effect. Future investigations on Fe-Ni alloys with different Ni contents using either of the pressure calibration method could help to further address this issue.

Besides the pressure dependence, we also investigated the effect of 10 wt.% nickel content in our sample on the temperature dependence of both bulk and shear moduli. For pure bcc-Fe, high temperature ultrasonic measurements have been conducted at ambient pressure (e.g., Adams et al. 2006; Dever 1972; Isaak and Masuda 1995; Leese and Lord Jr 1968) and high pressure (Shibazaki et al. 2016), the reported temperature dependence ranges from -0.029 GPa/K ~ -0.046 GPa/K for the bulk modulus ($\partial K_{S0}/\partial T$) and -0.015 GPa/K ~ -0.034 GPa/K for the shear modulus ($\partial G_0/\partial T$). Our results of $\partial K_{S0}/\partial T$ = -0.028(1) GPa/K and $\partial G_0/\partial T$ = -0.023(1) GPa/K for bcc-$Fe_{90}Ni_{10}$ are only marginally consistent with the lowest values reported for bcc-Fe, indicating that

10 wt.% nickel alloying with Fe can weakly affect the temperature dependence of both bulk and shear moduli.

The current adiabatic value of $\partial K_{S0}/\partial T$ = -0.028(1) GPa/K can be converted to its isothermal counterpart using the differentiated form of the thermodynamic identity $K_T = K_S/(1 + \alpha\gamma T)$, yielding $\partial K_{T0}/\partial T$ = -0.038(1) GPa/K. Two pressure-volume-temperature (*P-V-T*) investigations have reported $\partial K_{T0}/\partial T$ on bcc-Fe based on X-ray diffraction (XRD) studies and the results are largely discrepant. While Huang et al. (1987) reported a relatively small temperature dependence [$\partial K_{T0}/\partial T$ = -0.010(16) GPa/K], Zhang and Guyot (1999) provided a much larger value [$\partial K_{T0}/\partial T$ = -0.049(6) GPa/K], which is more consistent with the current ultrasonic results. To the authors' best knowledge, no *P-V-T* investigation on bcc-Fe-Ni alloy has yet been reported to provide a direct comparison with the current result.

5. Implications

Due to the limited coverage in pressure and temperature, our experimental results of velocities are not directly applicable to the Earth's core. We discuss possible implications for other phases, such as hcp-Fe-Ni systems, by investigating how the elastic properties are affected by nickel at high pressure and temperature. We found that the effect of nickel content on P and S wave velocities observed on bcc phase in this study is roughly consistent with the previously reported results on hcp Fe-Ni alloys (Lin et al. 2003; Morrison et al. 2019; Wakamatsu et al. 2018). This nickel effect could lead to a velocity decrease as large as ΔV_P = 0.8 km/s at inner core boundary (ICB) for hcp phase, as calculated by Ohtani et al. (2013), suggesting that nickel content plays as an important factor when we modelling the velocity structure of Earth's core to place constraints on its composition. From our measurements, we observed $(\partial V_P/\partial T)_\rho$ = -0.18(2) km/(s·10^3K) for

bcc-$Fe_{90}Ni_{10}$ at a constant density in current *P-T* range. In comparison, the $(\partial V_P/\partial T)_\rho$ for bcc-Fe varies from -0.33(4) km/(s·10^3K) to -0.37(3) km/(s·10^3K) by UI (Shibazaki et al. 2016) and IXS (Liu et al. 2014) measurements, respectively, indicating the nickel content can also reduce the effect of temperature on the V_P-ρ relationship. This implies that the use of temperature derivatives of Fe would produce an upper bound or overestimated value of velocity decrease (ΔV_P) at Earth's core conditions. Furthermore, we also observed a slightly smaller temperature effect of shear velocity in bcc-$Fe_{90}Ni_{10}$ [$(\partial V_S/\partial T)_\rho$ = -0.28(2) km/(s·10^3K)] than bcc-Fe [$(\partial V_S/\partial T)_\rho$ = -0.39(3) km/(s·10^3K)]. The low value of $(\partial V_S/\partial T)_\rho$ would introduce even larger V_S of hcp-Fe-Ni than previous estimations, which would require a more significant pre-melting effects (Martorell et al. 2013) or other mechanisms to account for the discrepancy of shear waves with the seismological observations. Thus, the decrease in the temperature effect induced by nickel alloying needs to be further evaluated in other structures of Fe-Ni alloys in an expanded *P-T* range; a better and more precise understanding of the Earth's core should take the effect of nickel into consideration instead of just ignoring it. Future acoustic measurements of both V_P and V_S of various Fe-Ni-light elements alloys and compounds at simultaneous high *P-T* conditions are also needed to provide a more comprehensive understanding of the composition and thermal structure of Earth's and planetary cores.

Acknowledgements

The authors would like to thank Jim Quinn for assistant with SEM at Stony Brook University. We also thank Robert. C. Liebermann for valuable discussions of this manuscript. We appreciate the constructive comments and suggestions of two anonymous reviewers. This project is supported by National Science Foundation (EAR-1524078) and DOE-NNSA (DE-NA0003886).

References

Adams, J.J., Agosta, D.S., Leisure, R.G., and Ledbetter, H. (2006) Elastic constants of monocrystal iron from 3 to 500 K. Journal of Applied Physics, 100(11), 113530.

Antonangeli, D., Komabayashi, T., Occelli, F., Borissenko, E., Walters, A., Fiquet, G., and Fei, Y. (2012) Simultaneous sound velocity and density measurements of hcp iron up to 93 GPa and 1100 K: An experimental test of the Birch's law at high temperature. Earth and Planetary Science Letters, 331-332, 210-214.

Birch, F. (1952) Elasticity and constitution of the Earth interior. Journal of Geophysical Research, 57(2), 227-286.

Birch, F. (1964) Density and composition of the mantle and the core. Journal of Geophysical Research, 69(20), 4377-4388.

Chigarev, N., Zinin, P., Ming, L.C., Amulele, G., Bulou, A., and Gusev, V. (2008) Laser generation and detection of longitudinal and shear acoustic waves in a diamond anvil cell. Applied Physics Letters, 93(18), 181905.

Davies, G.F., and Dziewonski, A.M. (1975) Homogeneity and constitution of Earth's lower mantle and outer core. Physics of the Earth and Planetary Interiors, 10(4), 336-343.

Decremps, F., Antonangeli, D., Gauthier, M., Ayrinhac, S., Morand, M., Marchand, G.L., Bergame, F., and Philippe, J. (2014) Sound velocity of iron up to 152 GPa by picosecond acoustics in diamond anvil cell. Geophysical Research Letters, 41(5), 1459-1464.

Dever, D.J. (1972) Temperature dependence of the elastic constants in α-iron single crystals: relationship to spin order and diffusion anomalies. Journal of Applied Physics, 43(8), 3293-3301.

Dubrovinsky, L., Dubrovinskaia, N., Narygina, O., Kantor, I., Kuznetzov, A., Prakapenka, V.B., Vitos, L., Johansson, B., Mikhaylushkin, A.S., Simak, S.I., and Abrikosov, I.A. (2007) Body-centered cubic iron-nickel alloy in Earth's core. Science, 316(5833), 1880-1883.

Dziewonski, A.M., and Anderson, D.L. (1981) Preliminary reference Earth model. Physics of the Earth and Planetary Interiors, 25(4), 297-356.

Fiquet, G., Badro, J., Guyot, F., Requardt, H., and Krisch, M. (2001) Sound velocities in iron to 110 gigapascals. Science, 291(5503), 468-71.

Gleason, A.E., Mao, W.L., and Zhao, J.Y. (2013) Sound velocities for hexagonally close-packed iron compressed hydrostatically to 136 GPa from phonon density of states. Geophysical Research Letters, 40(12), 2983-2987.

Huang, E., Bassett, W.A., and Tao, P. (1987) Pressure-temperature-volume relationship for hexagonal close packed iron determined by synchrotron radiation. Journal of Geophysical Research, 92(B8), 8129-8135.

Huang, E., Bassett, W.A., and Weathers, M. (1988) Phase relationships in Fe-Ni alloys at high pressures and temperatures. Journal of Geophysical Research, 93(B7), 7741-7746.

Isaak, D.G., and Masuda, K. (1995) Elastic and viscoelastic properties of α iron at high temperatures. Journal of Geophysical Research: Solid Earth, 100(B9), 17689-17698.

Kantor, A.P., Kantor, I.Y., Kurnosov, A.V., Kuznetsov, A.Y., Dubrovinskaia, N.A., Krisch, M., Bossak, A.A., Dmitriev, V.P., Urusov, V.S., and Dubrovinsky, L.S. (2007) Sound wave velocities of fcc Fe–Ni alloy at high pressure and temperature by mean of inelastic X-ray scattering. Physics of the Earth and Planetary Interiors, 164(1-2), 83-89.

Kuwayama, Y., Hirose, K., Sata, N., and Ohishi, Y. (2008) Phase relations of iron and iron–nickel alloys up to 300 GPa: Implications for composition and structure of the Earth's inner core. Earth and Planetary Science Letters, 273(3-4), 379-385.

Leese, J., and Lord Jr, A.E. (1968) Elastic stiffness coefficients of single-crystal iron from room temperature to 500 °C. Journal of Applied Physics, 39(8), 3986-3988.

Li, B., Chen, K., Kung, J., Liebermann, R.C., and Weidner, D.J. (2002) Sound velocity measurement using transfer function method. Journal of Physics-Condensed Matter, 14(44), 11337-11342.

Li, B., Kung, J., and Liebermann, R.C. (2004) Modern techniques in measuring elasticity of Earth materials at high pressure and high temperature using ultrasonic interferometry in conjunction with synchrotron X-radiation in multi-anvil apparatus. Physics of the Earth and Planetary Interiors, 143-144, 559-574.

Li, B., Liebermann, R.C., and Weidner, D.J. (2001) P-V-Vp-Vs-Tmeasurements on wadsleyite to 7 GPa and 873 K: Implications for the 410-km seismic discontinuity. Journal of Geophysical Research: Solid Earth, 106(B12), 30579-30591.

Li, B., and Zhang, J. (2005) Pressure and temperature dependence of elastic wave velocity of $MgSiO_3$ perovskite and the composition of the lower mantle. Physics of the Earth and Planetary Interiors, 151(1-2), 143-154.

Li, J., and Fei, Y. (2014) Experimental constraints on core composition. Treatise on geochemistry (2nd edition), 3, 527-557.

Lin, J.F., Struzhkin, V.V., Sturhahn, W., Huang, E., Zhao, J., Hu, M.Y., Alp, E.E., Mao, H.k., Boctor, N., and Hemley, R.J. (2003) Sound velocities of iron-nickel and iron-silicon alloys at high pressures. Geophysical Research Letters, 30(21), 2112.

Lin, J.F., Sturhahn, W., Zhao, J.Y., Shen, G.Y., Mao, H.K., and Hemley, R.J. (2005) Sound velocities of hot dense iron: Birch's law revisited. Science, 308(5730), 1892-1894.

Liu, J., Lin, J.F., Alatas, A., and Bi, W. (2014) Sound velocities of bcc-Fe and $Fe_{0.85}Si_{0.15}$ alloy at high pressure and temperature. Physics of the Earth and Planetary Interiors, 233, 24-32.

Mao, H.K., Shu, J., Shen, G., Hemley, R.J., Li, B., and Singh, A.K. (1998) Elasticity and rheology of iron above 220 GPa and the nature of the Earth's inner core. Nature, 396(6713), 741-743.

Mao, H.K., Wu, Y., Chen, L.C., Shu, J.F., and Jephcoat, A.P. (1990) Static compression of iron to 300 GPa and $Fe_{0.8}Ni_{0.2}$ alloy to 260 GPa: Implications for composition of the core. Journal of Geophysical Research, 95(B13), 21737-21742.

Mao, Z., Lin, J.F., Liu, J., Alatas, A., Gao, L., Zhao, J., and Mao, H.K. (2012) Sound velocities of Fe and Fe-Si alloy in the Earth's core. Proceedings of the National Academy of Sciences, 109(26), 10239-44.

Martorell, B., Vocadlo, L., Brodholt, J., and Wood, I.G. (2013) Strong premelting effect in the elastic properties of hcp-Fe under inner-core conditions. Science, 342(6157), 466-8.

Mcdonough, W.F., and Sun, S.S. (1995) The composition of the Earth. Chemical Geology, 120(3-4), 223-253.

Morrison, R.A., Jackson, J.M., Sturhahn, W., Zhang, D., and Greenberg, E. (2018) Equations of state and anisotropy of Fe-Ni-Si alloys. Journal of Geophysical Research: Solid Earth, 123(6), 4647-4675.

Morrison, R.A., Jackson, J.M., Sturhahn, W., Zhao, J., and Toellner, T.S. (2019) High pressure thermoelasticity and sound velocities of Fe-Ni-Si alloys. Physics of the Earth and Planetary Interiors, 294, 106268.

Murphy, C.A., Jackson, J.M., and Sturhahn, W. (2013) Experimental constraints on the thermodynamics and sound velocities of hcp-Fe to core pressures. Journal of Geophysical Research: Solid Earth, 118(5), 1999-2016.

Ohtani, E., Shibazaki, Y., Sakai, T., Mibe, K., Fukui, H., Kamada, S., Sakamaki, T., Seto, Y., Tsutsui, S., and Baron, A.Q.R. (2013) Sound velocity of hexagonal close-packed iron up to core pressures. Geophysical Research Letters, 40(19), 5089-5094.

Pommier, A. (2020) Experimental investigation of the effect of nickel on the electrical resistivity of Fe-Ni and Fe-Ni-S alloys under pressure. American Mineralogist, 105(7), 1069-1077.

Quareni, F., and Mulargia, F. (1988) The validity of the common approximate expressions for the Grüneisen parameter. Geophysical Journal International, 93(3), 505-519.

Sakai, T., Ohtani, E., Hirao, N., and Ohishi, Y. (2011) Stability field of the hcp-structure for Fe, Fe-Ni, and Fe-Ni-Si alloys up to 3 Mbar. Geophysical research letters, 38(9), L09302.

Shibazaki, Y., Nishida, K., Higo, Y., Igarashi, M., Tahara, M., Sakamaki, T., Terasaki, H., Shimoyama, Y., Kuwabara, S., Takubo, Y., and Ohtani, E. (2016) Compressional and shear wave velocities for polycrystalline bcc-Fe up to 6.3 GPa and 800 K. American Mineralogist, 101(5), 1150-1160.

Stixrude, L. (2012) Structure of Iron to 1 Gbar and 40 000 K. Physical Review Letters, 108(5), 055505.

Takahashi, T., Bassett, W.A., and Mao, H.K. (1968) Isothermal compression of the alloys of iron up to 300 kilobars at room temperature: Iron-nickel alloys. Journal of Geophysical Research, 73(14), 4717-4725.

Tateno, S., Hirose, K., Komabayashi, T., Ozawa, H., and Ohishi, Y. (2012) The structure of Fe-Ni alloy in Earth's inner core. Geophysical Research Letters, 39(12), L12305.

Tateno, S., Hirose, K., Ohishi, Y., and Tatsumi, Y. (2010) The structure of iron in Earth's inner core. Science, 330(6002), 359-361.

Vocadlo, L., Alfe, D., Gillan, M.J., Wood, I.G., Brodholt, J.P., and Price, G.D. (2003) Possible thermal and chemical stabilization of body-centred-cubic iron in the Earth's core. Nature, 424(6948), 536-539.

Wakamatsu, T., Ohta, K., Yagi, T., Hirose, K., and Ohishi, Y. (2018) Measurements of sound velocity in iron–nickel alloys by femtosecond laser pulses in a diamond anvil cell. Physics and Chemistry of Minerals, 45(6), 589-595.

Wang, X., Chen, T., Qi, X., Zou, Y., Kung, J., Yu, T., Wang, Y., Liebermann, R.C., and Li, B. (2015) Acoustic travel time gauges for in-situ determination of pressure and temperature in multi-anvil apparatus. Journal of Applied Physics, 118(6), 065901.

Zhang, J., and Guyot, F. (1999) Thermal equation of state of iron and $Fe_{0.91}Si_{0.09}$. Physics and Chemistry of Minerals, 26(3), 206-211.

405 **Table 1** Experimental (P, T, $2t_P$, $2t_S$) and calculated (Length, ρ, V_P, V_S, K_S, G) data of bcc-$Fe_{90}Ni_{10}$

P (GPa)	T (K)	$2t_P$ (μs)	$2t_S$ (μs)	Length (mm)	ρ (g/cm^3)	V_P (km/s)	V_S (km/s)	K_S (GPa)	G (GPa)
6.2	323	0.3080(2)	0.5816(28)	0.9148	8.246	5.94(6)	3.15(3)	182.2(33)	81.6(11)
7.6	776	0.3188(4)	0.6188(18)	0.9174	8.176	5.76(6)	2.97(3)	175.0(30)	71.9(8)
7.4	667	0.3150(4)	0.6060(4)	0.9165	8.200	5.82(6)	3.02(3)	177.6(30)	75.0(8)
7.1	570	0.3124(4)	0.5968(8)	0.9160	8.212	5.86(6)	3.07(3)	179.2(31)	77.4(8)
6.7	472	0.3104(2)	0.5868(22)	0.9155	8.228	5.90(6)	3.12(3)	179.5(32)	80.1(10)
6.1	328	0.3080(4)	0.5810(28)	0.9149	8.243	5.94(6)	3.15(3)	181.9(34)	81.8(11)
5.6	322	0.3092(4)	0.5828(22)	0.9157	8.220	5.92(6)	3.14(3)	180.2(33)	81.2(10)
6.9	785	0.3210(12)	0.6208(16)	0.9188	8.140	5.72(6)	2.96(3)	171.6(35)	71.3(8)
6.8	674	0.3172(6)	0.6096(8)	0.9177	8.167	5.79(6)	3.01(3)	174.7(31)	74.0(8)
6.6	576	0.3146(8)	0.5990(10)	0.9170	8.186	5.83(6)	3.06(3)	175.9(33)	76.7(8)
6.2	470	0.3120(2)	0.5900(10)	0.9165	8.201	5.87(6)	3.11(3)	177.5(31)	79.1(8)
5.6	329	0.3098(2)	0.5826(28)	0.9158	8.219	5.91(6)	3.14(3)	179.0(33)	81.2(11)
4.3	309	0.3140(4)	0.5864(12)	0.9178	8.165	5.85(6)	3.13(3)	172.4(31)	80.0(9)
5.6	782	0.3256(2)	0.6244(6)	0.9213	8.073	5.66(6)	2.95(3)	164.8(28)	70.3(7)
5.4	661	0.3214(2)	0.6130(4)	0.9201	8.103	5.73(6)	3.00(3)	168.3(29)	73.0(7)
5.2	573	0.3192(2)	0.6050(2)	0.9195	8.121	5.76(6)	3.04(3)	169.5(29)	75.0(8)
4.9	468	0.3172(2)	0.5984(2)	0.9188	8.139	5.79(6)	3.07(3)	170.8(29)	76.7(8)
4.3	316	0.3150(2)	0.5878(10)	0.9181	8.158	5.83(6)	3.12(3)	171.0(30)	79.6(8)
2.6	310	0.3206(4)	0.6010(18)	0.9211	8.077	5.75(6)	3.07(3)	165.5(30)	75.9(9)
3.1	779	0.3336(2)	0.6406(8)	0.9260	7.950	5.55(6)	2.89(3)	156.4(26)	66.4(7)
2.9	673	0.3300(2)	0.6268(20)	0.9251	7.974	5.61(6)	2.95(3)	158.0(28)	69.5(8)
2.8	571	0.3266(4)	0.6188(26)	0.9240	8.002	5.66(6)	2.99(3)	161.1(29)	71.4(9)
2.7	474	0.3244(4)	0.6134(38)	0.9229	8.030	5.69(6)	3.01(3)	163.0(31)	72.7(12)
2.3	318	0.3218(2)	0.6028(14)	0.9217	8.062	5.73(6)	3.06(3)	164.0(29)	75.4(8)
3.2	776	0.3334(2)	0.6352(16)	0.9259	7.952	5.55(6)	2.92(3)	155.2(27)	67.6(8)
3.0	674	0.3302(2)	0.6244(4)	0.9249	7.978	5.60(6)	2.96(3)	157.0(27)	70.0(7)
2.8	571	0.3270(2)	0.6188(22)	0.9239	8.003	5.65(6)	2.99(3)	160.4(28)	71.4(9)
2.8	473	0.3246(2)	0.6114(4)	0.9229	8.031	5.69(6)	3.02(3)	162.1(28)	73.2(7)
2.5	343	0.3226(2)	0.6050(10)	0.9218	8.060	5.71(6)	3.05(3)	163.4(29)	74.8(8)

Note: The uncertainty of length calculated in this study is approximately ±1%.

406

This is the peer-reviewed, final accepted version for American Mineralogist, published by the Mineralogical Society of America.
The published version is subject to change. Cite as Authors (Year) Title. American Mineralogist, in press.
DOI: https://doi.org/10.2138/am-2021-7716. http://www.minsocam.org/

407 **Table 2** Comparison of thermoelastic properties of bcc-Fe and bcc-Fe-Ni alloys

Reference		P range	T range	K_{S0}	$\partial K_{S0}/\partial P$	$\partial K_{S0}/\partial T$	G_0	$\partial G_0/\partial P$	$\partial G_0/\partial T$	K_{T0}	$\partial K_{T0}/\partial P$	$\partial K_{T0}/\partial T$	EOS	Notes
		(GPa)	(K)	(GPa)		(GPa/K)	(GPa)		(GPa/K)	(GPa)		(GPa/K)		
This study	$Fe_{90}Ni_{10}$	~8	~773	154.2(8)	4.6(2)	-0.028(1)	73.2(2)	1.5(1)	-0.023(1)	–	–	–	3rd Finite strain	Ultrasonic, adiabatic
			~673	153.8(7)	4.7(2)	-0.027(2)	72.7(2)	1.6(1)	-0.022(1)	–	–	–		
Shibazaki et al. (2016)	Fe	~6.3	~800	163.2(15)	6.75(33)	–0.038(3)	81.4(6)	1.66(14)	-0.029	–	–	–	Polynomial	Ultrasonic, adiabatic
Adams et al. (2006)	Fe	0	~500	166.2	–	-0.029	81.5[a]	–	-0.025	–	–	–	–	Ultrasonic, adiabatic
Isaak and Masuda (1995)	Fe	0	~800	165.7	–	-0.046	82.0[a]	–	-0.034	–	–	–	–	Ultrasonic, adiabatic
Dever (1972)	Fe	0	~773	167.8	–	-0.035	82.0[a]	–	-0.029	–	–	–	–	Ultrasonic, adiabatic
Leese and Lord (1968)	Fe	0	~773	168.7	–	-0.041	77.9[a]	–	-0.015	–	–	–	–	Ultrasonic, adiabatic
Zhang and Guyot (1999)	Fe	~9	~773	–	–	–	–	–	–	155(2)	5.3[b]	-0.049(6)	3rd Birch Murnaghan	XRD, isothermal
Huang et al. (1987)	Fe	~12	~723	–	–	–	–	–	–	171(8)	4[b]	-0.010(16)	Birch Murnaghan	XRD, isothermal
Takahashi et al. (1968)	Fe	~15	300	–	–	–	–	–	–	162(5)	5.5(8)	–	Murnaghan	XRD, isothermal
	$Fe_{95}Ni_5$	~16	300	–	–	–	–	–	–	155(10)	4.2(8)	–		
	$Fe_{90}Ni_{10}$	~17	300	–	–	–	–	–	–	155(10)	5.7(8)	–		
Morrison et al. (2018)	$Fe_{91}Ni_{09}$	~15	300	–	–	–	–	–	–	146.8(31)	6.39(64)	–	3rd Birch Murnaghan	XRD, isothermal

408 Notes: [a]: Voigt-Reuss-Hill average; [b]: fixed value.

409

410 **Figure 1** Phase diagram of Fe-Ni alloy system at high *P-T* based on the data of Huang et al.
411 (1988). Solid dots indicate the experimental *P-T* conditions where the ultrasonic data were
412 acquired in this study.

413

414 **Figure 2** Scanning electron microscope image of sample after high temperature annealing.

415

416 **Figure 3** Sketch of the cell assembly used in current study for ultrasonic measurement.

417

418 **Figure 4** Signal example of (a) P wave and (b) S wave obtained at 7.6 GPa and 776 K.

419

420 **Figure 5** Compressional (V_P) and shear (V_S) wave velocities as a function of pressure and
421 temperature. Solid lines are the finite strain fitted curves from this study. Temperature
422 information are color coded and shown in legend.

423

424 **Figure 6** Bulk and shear modulus as a function of pressure and temperature. Solid lines are the
425 finite strain fitted curves from this study. Dashed lines are calculated from Shibazaki et al.
426 (2016). Temperature information are color coded and shown in legend.

This is the peer-reviewed, final accepted version for American Mineralogist, published by the Mineralogical Society of America.
The published version is subject to change. Cite as Authors (Year) Title. American Mineralogist, in press.
DOI: https://doi.org/10.2138/am-2021-7716. http://www.minsocam.org/

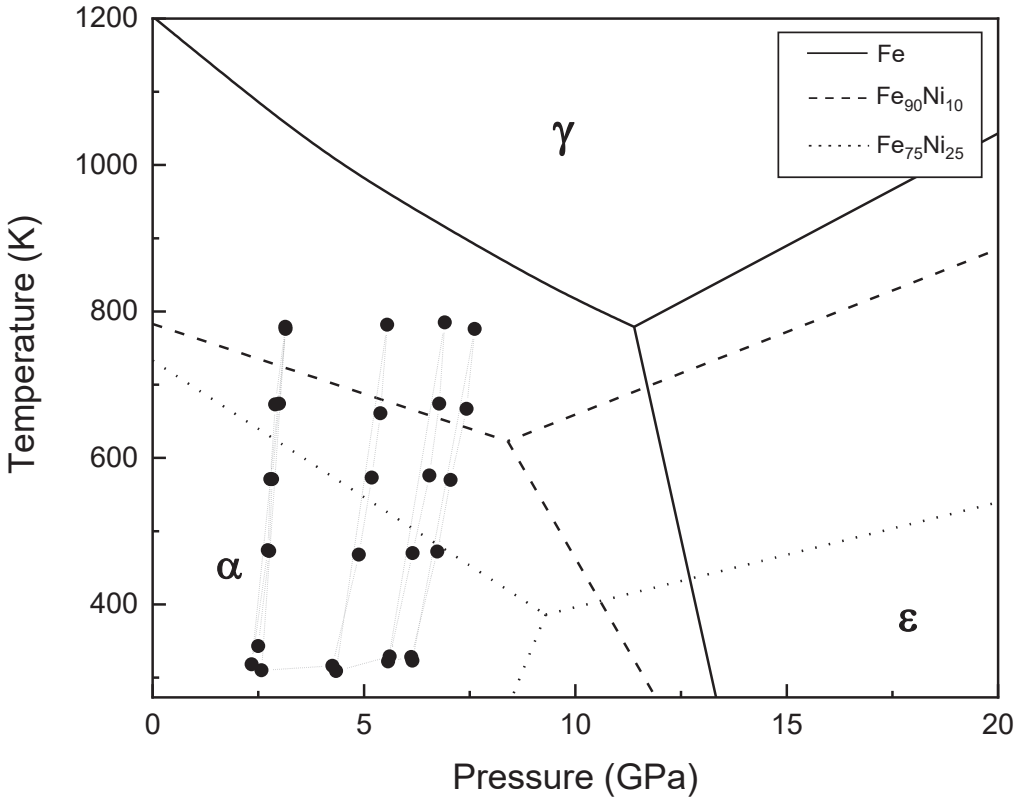

Figure 1

This is the peer-reviewed, final accepted version for American Mineralogist, published by the Mineralogical Society of America.
The published version is subject to change. Cite as Authors (Year) Title. American Mineralogist, in press.
DOI: https://doi.org/10.2138/am-2021-7716. http://www.minsocam.org/

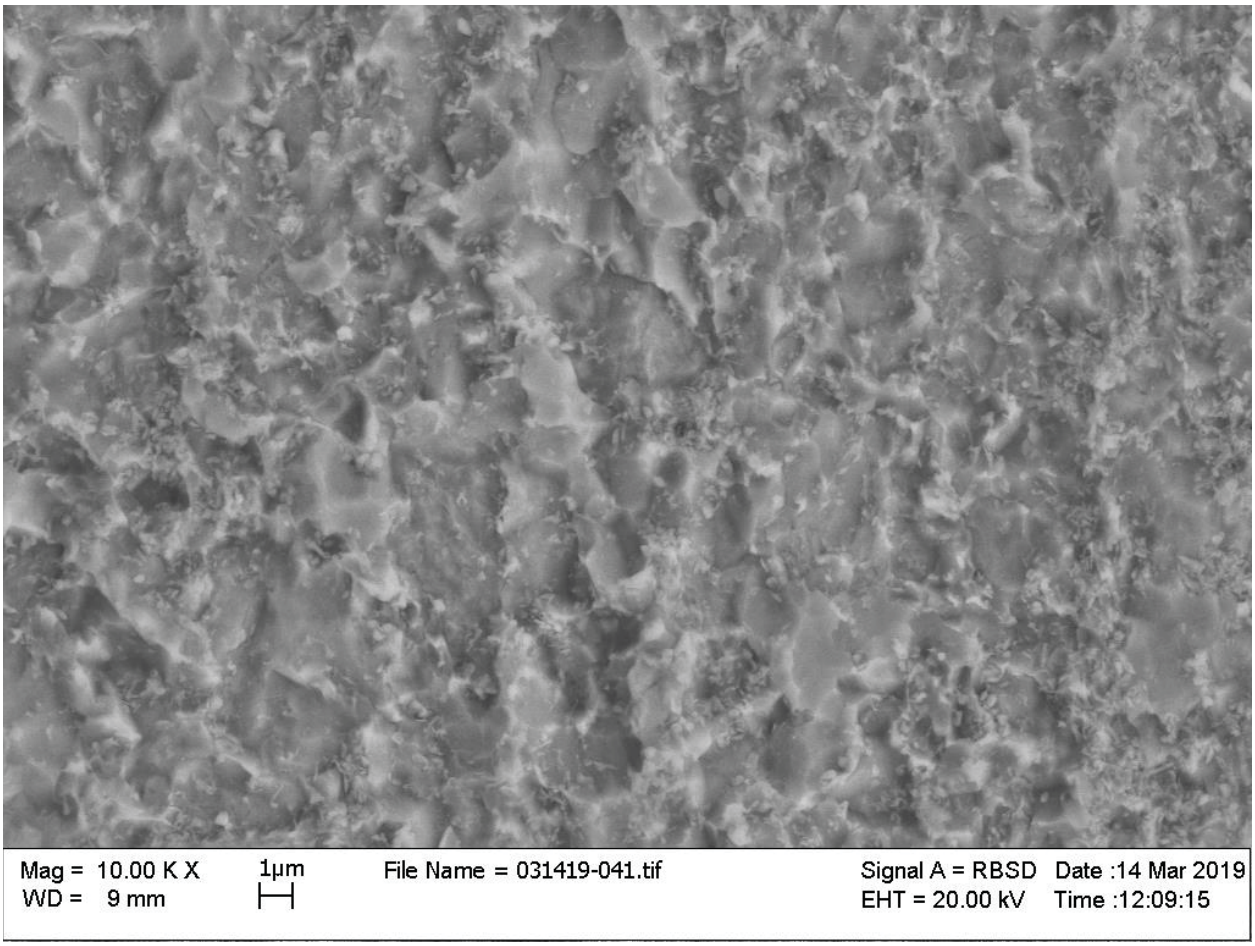

Figure 2

This is the peer-reviewed, final accepted version for American Mineralogist, published by the Mineralogical Society of America.
The published version is subject to change. Cite as Authors (Year) Title. American Mineralogist, in press.
DOI: https://doi.org/10.2138/am-2021-7716. http://www.minsocam.org/

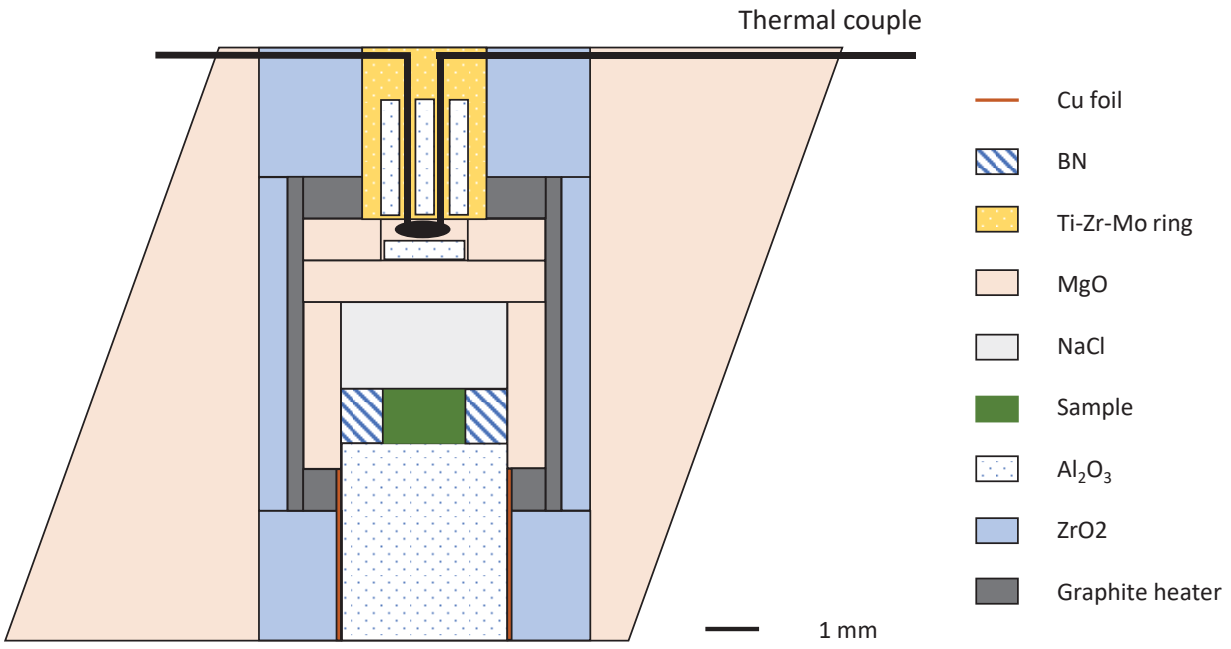

Figure 3

This is the peer-reviewed, final accepted version for American Mineralogist, published by the Mineralogical Society of America.
The published version is subject to change. Cite as Authors (Year) Title. American Mineralogist, in press.
DOI: https://doi.org/10.2138/am-2021-7716. http://www.minsocam.org/

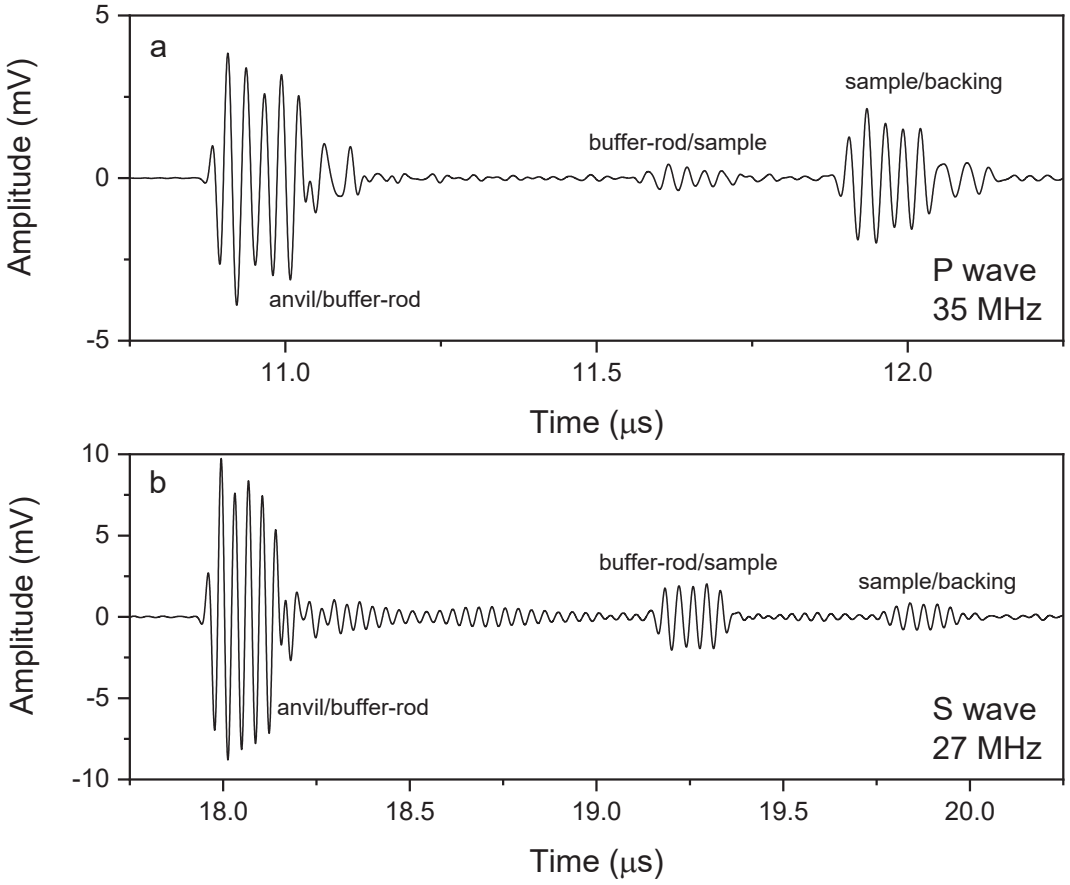

Figure 4

This is the peer-reviewed, final accepted version for American Mineralogist, published by the Mineralogical Society of America.
The published version is subject to change. Cite as Authors (Year) Title. American Mineralogist, in press.
DOI: https://doi.org/10.2138/am-2021-7716. http://www.minsocam.org/

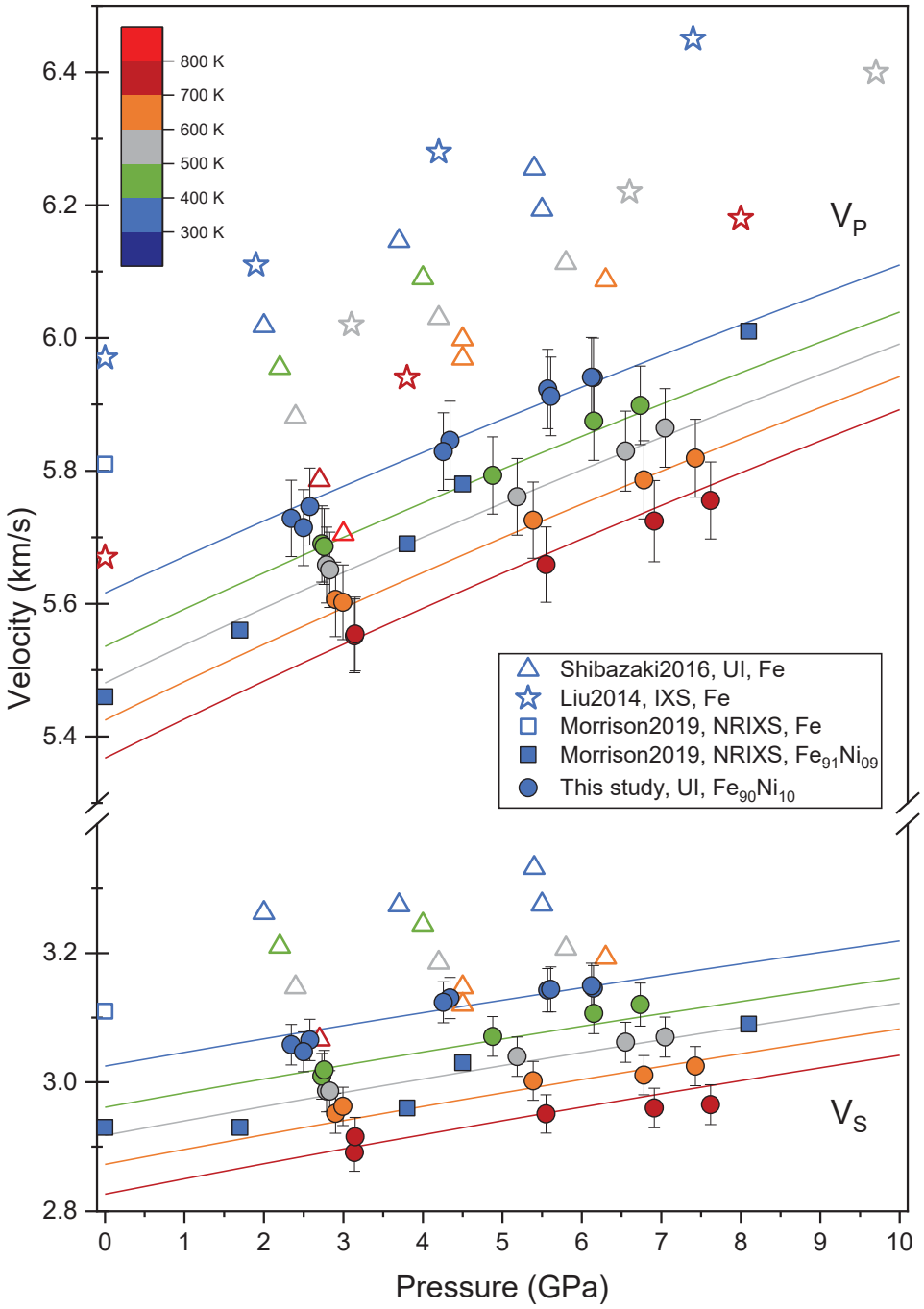

Figure 5

This is the peer-reviewed, final accepted version for American Mineralogist, published by the Mineralogical Society of America.
The published version is subject to change. Cite as Authors (Year) Title. American Mineralogist, in press.
DOI: https://doi.org/10.2138/am-2021-7716. http://www.minsocam.org/

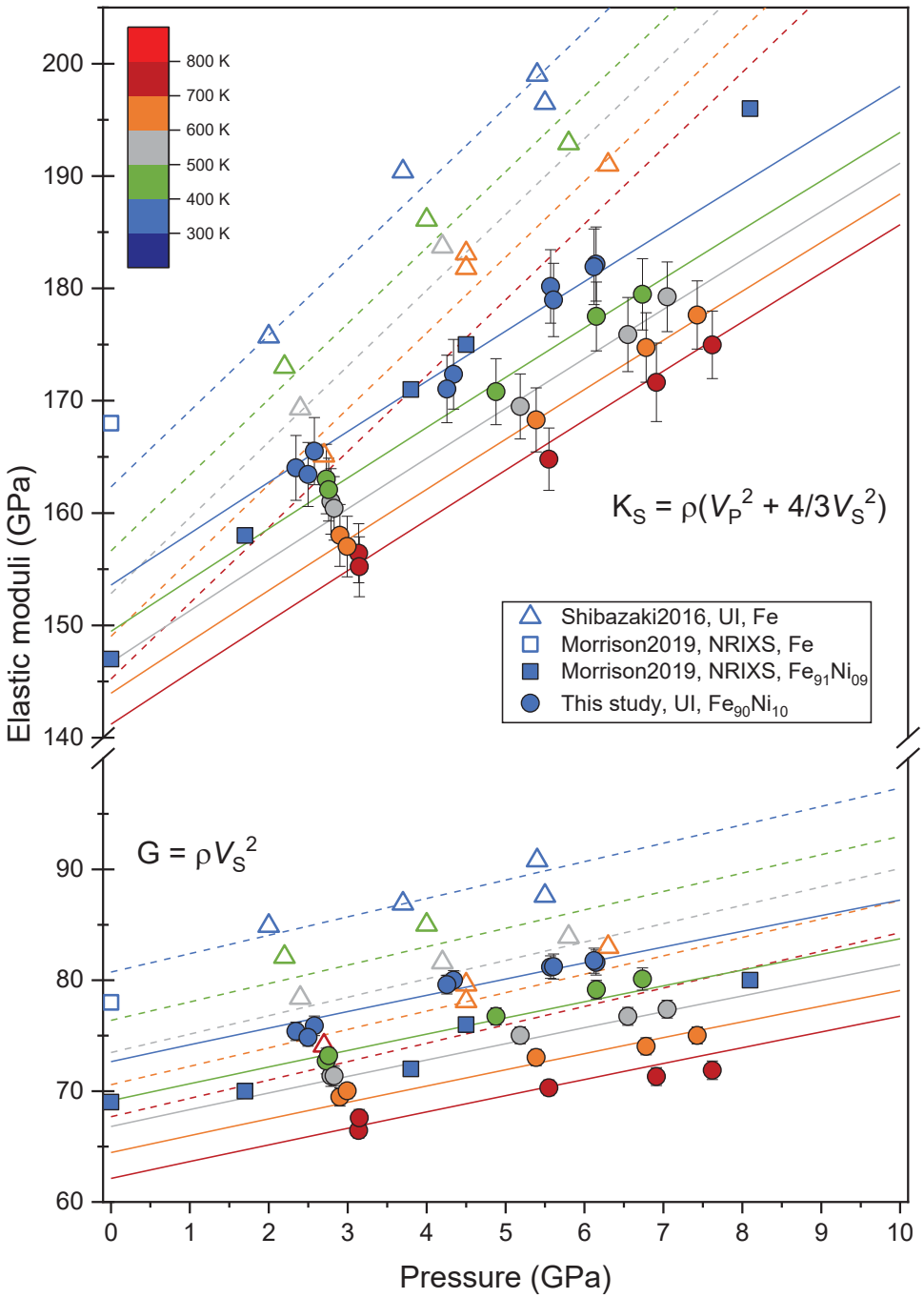

Figure 6